AN AIRBORNE LIDAR SCANNING AND MACHINE LEARNING SYSTEM FOR REAL-TIME EVENT EXTRACTION AND CONTROL POLICIES IN URBAN TRANSPORTATION NETWORKS

FINAL PROJECT REPORT

by

Christopher Parrish, David Hurwitz, and Chase Simpson
School of Civil and Construction Engineering
Oregon State University, Corvallis, Oregon, USA

Sameh Sorour, and Ahmed Abdel-Rahim
University of Idaho, Moscow, Idaho, USA

Sponsorship
Oregon Department of Transportation (ODOT) and National Institute for Advanced Transportation Technology (NIATT)

for

Pacific Northwest Transportation Consortium (PacTrans)
USDOT University Transportation Center for Federal Region 10
University of Washington
More Hall 112, Box 352700
Seattle, WA 98195-2700

In cooperation with U.S. Department of Transportation,
Office of the Assistant Secretary for Research and Technology (OST-R)

DISCLAIMER

The contents of this report reflect the views of the authors, who are responsible for the facts and the accuracy of the information presented herein. This document is disseminated under the sponsorship of the U.S. Department of Transportation's University Transportation Centers Program, in the interest of information exchange. The Pacific Northwest Transportation Consortium, the U.S. Government and matching sponsor assume no liability for the contents or use thereof.

TECHNICAL REPORT DOCUMENTATION PAGE

1. Report No.	2. Government Accession No.	3. Recipient's Catalog No.
	01701469	

4. Title and Subtitle	5. Report Date
AN AIRBORNE LIDAR SCANNING AND DEEP LEARNING SYSTEM FOR REAL-TIME EVENT EXTRACTION AND CONTROL POLICIES IN URBAN TRANSPORTATION NETWORKS	September 30, 2109
	6. Performing Organization Code

7. Author(s) and Affiliations	8. Performing Organization Report No.
Christopher Parrish, 0000-0002-2681-0090 –Oregon State University David Hurwitz, 0000-0001-8450-6516 and Chase Simpson – Oregon State University Sameh Sorour, and Ahmed Abdel-Rahim 0000-0001-9756-554X – University of Idaho	2017-M-OSU-3

9. Performing Organization Name and Address	10. Work Unit No. (TRAIS)
PacTrans Pacific Northwest Transportation Consortium University Transportation Center for Federal Region 10 University of Washington More Hall 112 Seattle, WA 98195-2700	**11. Contract or Grant No.** 69A3551747110

12. Sponsoring Organization Name and Address	13. Type of Report and Period Covered
United States Department of Transportation Research and Innovative Technology Administration 1200 New Jersey Avenue, SE Washington, DC 20590	Research **14. Sponsoring Agency Code**

15. Supplementary Notes

Report uploaded to: www.pactrans.org

16. Abstract

Airborne light detection and ranging (lidar) and unmanned aircraft systems (UAS), also called drones, are emerging technologies that are of growing interest for a range of transportation applications. At the same time, machine learning is leading to rapid advances in the ability to automatically extract actionable information from lidar data. This project investigated the combined use of UAS, lidar and machine learning for traffic network monitoring. A custom lidar-UAS was built, instrumented, and used to acquire data over multiple test sites. New processing algorithms were developed to automatically parse raw data, generate georeferenced point clouds, filter out repetitions, and perform scanning to identify vehicles, all with processors that can be mounted on UAS and operated in real-time. The results of the UAS lidar data collection were used to develop operational guidance for transportation agencies using UAS to collect lidar data in proximity to active roadways. Additionally, this work resulted in an end-to-end processing system, implemented in C++, capable of real-time vehicle recognition with processors that can be mounted on UAS. A final output of the project was a set of specific recommendations for follow-up research, contributing to the long-range vision for traffic networking monitoring using a fleet of UAS that can inform real-time decisions.

17. Key Words	18. Distribution Statement
Laser radar, drones, digital mapping, machine learning	

19. Security Classification (of this report)	20. Security Classification (of this page)	21. No. of Pages	22. Price
Unclassified.	Unclassified.		N/A

Form DOT F 1700.7 (8-72) **Reproduction of completed page authorized.**

SI* (MODERN METRIC) CONVERSION FACTORS

APPROXIMATE CONVERSIONS TO SI UNITS				
Symbol	**When You Know**	**Multiply By**	**To Find**	**Symbol**
		LENGTH		
in	inches	25.4	millimeters	mm
ft	feet	0.305	meters	m
yd	yards	0.914	meters	m
mi	miles	1.61	kilometers	km
		AREA		
in^2	square inches	645.2	square millimeters	mm^2
ft^2	square feet	0.093	square meters	m^2
yd^2	square yard	0.836	square meters	m^2
ac	acres	0.405	hectares	ha
mi^2	square miles	2.59	square kilometers	km^2
		VOLUME		
fl oz	fluid ounces	29.57	milliliters	mL
gal	gallons	3.785	liters	L
ft^3	cubic feet	0.028	cubic meters	m^3
yd^3	cubic yards	0.765	cubic meters	m^3
	NOTE: volumes greater than 1000 L shall be shown in m^3			
		MASS		
oz	ounces	28.35	grams	g
lb	pounds	0.454	kilograms	kg
T	short tons (2000 lb)	0.907	megagrams (or "metric ton")	Mg (or "t")
		TEMPERATURE (exact degrees)		
°F	Fahrenheit	5 (F-32)/9 or (F-32)/1.8	Celsius	°C
		ILLUMINATION		
fc	foot-candles	10.76	lux	lx
fl	foot-Lamberts	3.426	$candela/m^2$	cd/m^2
		FORCE and PRESSURE or STRESS		
lbf	poundforce	4.45	newtons	N
lbf/in^2	poundforce per square inch	6.89	kilopascals	kPa

APPROXIMATE CONVERSIONS FROM SI UNITS				
Symbol	**When You Know**	**Multiply By**	**To Find**	**Symbol**
		LENGTH		
mm	millimeters	0.039	inches	in
m	meters	3.28	feet	ft
m	meters	1.09	yards	yd
km	kilometers	0.621	miles	mi
		AREA		
mm^2	square millimeters	0.0016	square inches	in^2
m^2	square meters	10.764	square feet	ft^2
m^2	square meters	1.195	square yards	yd^2
ha	hectares	2.47	acres	ac
km^2	square kilometers	0.386	square miles	mi^2
		VOLUME		
mL	milliliters	0.034	fluid ounces	fl oz
L	liters	0.264	gallons	gal
m^3	cubic meters	35.314	cubic feet	ft^3
m^3	cubic meters	1.307	cubic yards	yd^3
		MASS		
g	grams	0.035	ounces	oz
kg	kilograms	2.202	pounds	lb
Mg (or "t")	megagrams (or "metric ton")	1.103	short tons (2000 lb)	T
		TEMPERATURE (exact degrees)		
°C	Celsius	1.8C+32	Fahrenheit	°F
		ILLUMINATION		
lx	lux	0.0929	foot-candles	fc
cd/m^2	$candela/m^2$	0.2919	foot-Lamberts	fl
		FORCE and PRESSURE or STRESS		
N	newtons	0.225	poundforce	lbf
kPa	kilopascals	0.145	poundforce per square inch	lbf/in^2

*SI is the symbol for the International System of Units. Appropriate rounding should be made to comply with Section 4 of ASTM E380.
(Revised March 2003)

TABLE OF CONTENTS

LIST OF FIGURES

LIST OF TABLES

LIST OF ABBREVIATIONS

DEM: Digital Elevation Models
FAA: Federal Aviation Administration
FOG: Fiber optic gyroscope
GNSS: Global Navigation Satellite System
INS: Inertial Navigation System
Lidar: Light Detection and Ranging
ODOT: Oregon Department of Transportation
OSU: Oregon State University
PacTrans: Pacific Northwest Transportation Consortium
UAS: Unmanned Aircraft System
UI: University of Idaho
WSDOT: Washington State Department of Transportation

ACKNOWLEDGMENTS

The project team gratefully acknowledges the contributions of Richard Slocum, Oregon State University PhD student, who assisted in building, instrumenting and testing the lidar-equipped unmanned aircraft system (UAS) used in this research, Chris Glantz, PLS, Deputy State Surveyor, Lead Remote Sensing Surveyor, and UAS Program Coordinator, Oregon Department of Transportation (ODOT), who facilitated the UAS- lidar data collection at Newberg-Dundee bypass construction site, and Jake Dafni, PhD, PE, Operations Manager, NHERI RABID Experimental Facility who facilitated the UAS- lidar data collection at the University of Washington.

EXECUTIVE SUMMARY

Unmanned aircraft systems (UAS), also called drones, and light detection and ranging (lidar) are rapidly emerging technologies, which are having a transformational effect on how mapping and monitoring are performed in a number of fields. Furthermore, machine learning is engendering rapid advances in automatic extraction of actionable information from imagery and point clouds. Together, these new acquisition and processing capabilities appear poised to revolutionize how data are collected for transportation applications, such as traffic network monitoring. However, myriad challenges remain. UAS-based lidar is a cutting-edge, and still relatively unproven, technology, with operational challenges ranging from sensor calibration to payload and flight time limitations. Machine learning algorithms that have been designed, implemented and tested in vastly different fields require adaptation for transportation use. In addition, regulatory and logistical issues are paramount, as FAA, state, and local regulations dictate how, when, where, and by whom UAS flights can be conducted, and operating UAS safely, effectively and in full compliance with all applicable laws, rules, and regulations requires training, preparation, and pre-planning. This project aimed to rigorously investigate and document both the state-of-the-art and the state-of-the-possible in performing traffic network monitoring with lidar-equipped UAS and machine learning algorithms. A lidar-UAS was built, instrumented and operated over three sites, ranging from a highly-controlled test environment to alongside an active roadway with heavy traffic, with flights conducted by Federal Aviation Administration (FAA) Part 107 certified remote pilots. Additionally, a fourth site, covering an intersection on the University of Washington campus, was flown with a higher-end UAS lidar system. Novel processing algorithms were used to automatically parse raw data into georeferenced point clouds, filter out repetitions, and perform scanning to identify vehicles, all with processors that can be mounted on UAS and operated in real-time. The UAS lidar acquisition performed in this project led to a follow-on PacTrans Success Stories project and resulted in a report documenting current best practices in operational UAS for transportation applications. Meanwhile, the machine learning aspects of the study have led to the ability to identify vehicles using drone-mountable hardware and algorithms. Recommendations for future work include testing the approach using boards with even smaller computational power, enhancing the point cloud and reference vehicle filtering, and investigating new types of remote aircraft with greater endurance.

CHAPTER 1. INTRODUCTION

1.1. Background

Two technologies that are having a dramatic impact on surveying, mapping and monitoring are light detection and ranging (lidar) and unmanned aircraft systems (UAS). Of the two, lidar is arguably the more mature technology, having first become commercially available for surveying and mapping in the mid-to late-1990s and proliferating rapidly over the past two decades (Nayegandhi and Nimetz, 2018). Lidar uses laser ranges—often obtained from a moving survey platform, such as an airplane or truck—combined with pointing angle information, global navigation satellite system (GNSS) and inertial navigation system (INS) data to produce dense 3D point clouds. From the point clouds, downstream data products, including digital elevation models (DEMs), elevation contours, building models, and others, can be produced. Unmanned aircraft systems (UAS), also called drones, have emerged into the commercial market somewhat more recently, but are rapidly gaining recognition as an operationally-viable tool for surveying, mapping and monitoring applications. Commercial use of UAS was greatly facilitated in 2016, when the Federal Aviation Administration (FAA) released regulations for small (< 55 lb) unmanned aircraft: 14 CFR Part 107 (FAA, 2016), referred to simply as "Part 107" throughout the remainder of this report.

Meanwhile, machine learning is having similarly transformative impacts on how information is extracted from the huge volumes of lidar and imagery now being collected. Machine learning algorithms provide the capability to identify features and objects in data representation, lidar scans in our case, and can be employed by government agencies to make better decisions from the data. Although machine learning was classically a centralized technique, where data are analyzed after being transferred to central high-performance computing facilities, recent trends aim to implement machine-learning algorithms at or close to the data generation units, especially for real-time monitoring and applications. This direction is motivated by the huge size of the data, whose transmission can take a very long time and drain significant resources. Instead of sending the data, these "edge"-type lightweight machine learning approaches can extract basic objects and features, which are typically substantially smaller than the raw data, and send those in real-time. This approach is well suited for energy-constrained devices that are required to provide real-time information, and, therefore, cannot wait for data collection. Clearly, this is exactly the situation encountered in a real-time monitoring application using battery-powered UAS.

The combination of lidar, UAS, and machine learning could be a game changer for a number of transportation applications. One such application is traffic network monitoring. It is envisioned that in the future, a traffic network could be monitored by a fleet of lidar-equipped UAS (Figure 1.1). Through the use of machine learning algorithms, features of interest could be automatically detected and identified, including those relevant to emergency response, clearance, congestion, accidents, fire, parking utilization, and multimodal transportation activities. If the feature extraction were to be accomplished in real time, the obtained results could be cooperatively reported to a traffic network controller, informing corresponding actions.

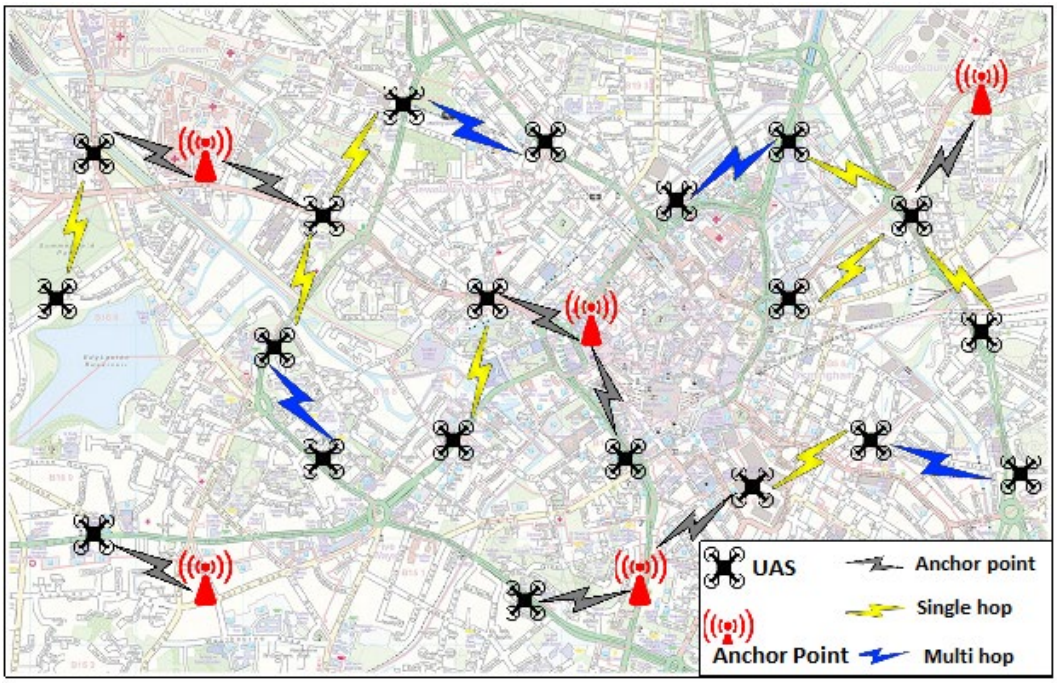

Figure 1.1 An example of UAS and anchor point distribution, and single/multi hop communications among them to relay their information to the anchor points.

While the vision outlined above is compelling, a number of technical and logistical challenges must be overcome for it to be achievable. Lidar systems with low enough size, weight and power consumption to be suitable for UAS installation have only recently become available (Jozkow et al., 2016), and their performance is still largely untested. Furthermore, for lidar points to be assigned accurate 3D spatial coordinates (latitudes, longitudes, and heights or, in a projected coordinate system, eastings, northings, and heights), a direct georeferencing system, consisting of a global navigation satellite system (GNSS) aided inertial navigation system (INS) is needed. This direct georeferencing system add additional weight and processing requirements. Machine learning algorithms specifically for automatic extraction of features from UAS-lidar must be developed and tested.

However, the greatest challenges pertain not to technical issues, but, rather, logistical and regulatory constraints (Stöcker et al., 2017; Collins et al., 2018; Parrish et al., 2018). Flights conducted under FAA Part 107 must adhere to all applicable rules, and state transportation agencies may have their own restrictions, such as how far from an active roadway a UAS can be operated. Specific guidance is needed for State DOTs and other transportation agencies to collect UAS lidar data in the vicinity of active roadways in a manner that meets all applicable rules, regulations, safety protocols, and provides accurate data from which actionable information can be extracted.

1.2. Research Objectives

Based on the long-range vision and challenges presented above, the overarching goal of this project was to develop and test procedures for using lidar-UAS, combined with machine learning, for traffic network monitoring. Specific objectives of the project were to: 1) optimize mission parameters for UAS-based

lidar acquisition for traffic network monitoring; 2) design, implement and train a convolutional layer for automatically extracting features from the UAS-based lidar data; 3) investigate operational strategies that will, in the future, enable fleets of UAS to work collaboratively to scan a transportation network; and 4) develop guidelines for State DOTs and other transportation agencies on the technical and operational requirements for UAS-based lidar acquisition.

CHAPTER 2. DEVELOPMENT AND TESTING OF LIDAR-UAS

2.1. Justification for lidar

A fundamental question, which was carefully considered at the outset of this project, is: *why use lidar?* Image-based mapping techniques, which are able to reconstruct 3D geometry from overlapping sets of imagery acquired from a UAS or other platform, are gaining wide acceptance. In particular, structure from motion (SfM), a new type of photogrammetric software leveraging advances from the field of computer vision (Fonstad et al., 2013; Westoby et al., 2012; Tonkin et al., 2014), has emerged as a highly-effective technique for creating accurate, spatially dense 3D point clouds from imagery acquired from UAS. To address this question, a qualitative comparison of UAS-SfM and UAS-lidar was conducted (Simpson, 2018). Results of this comparison are summarized in Table 2.1. It is worth noting that a major obstacle that was not considered in the comparison is that SfM processing for real-time traffic monitoring is not currently feasible, as the processing to derive a dense point cloud can take anywhere from several minutes to several hours depending on the size of the dataset and the computing power available. On the other hand, with appropriate on-board processing hardware and software, lidar can achieve better than 1:1 processing:acquisition time ratios, making it suitable for real-time monitoring.

Table 2.1 Summary of the qualitative comparisons between UAS- lidar and UAS-SfM as conducted by Simpson, 2018 (included and modified with permissions from author).

	UAS- lidar	**UAS-SfM**
Cost	high	low
Acquisition time	low	low
User-input processing time	high	moderate
Demand on computing resources	moderate	high
Operational expertise required	high	low
Processing expertise required	high	low
Sensor type	lidar (active)	RGB camera (passive)
Variables of each data point	position & intensity	position & RGB
Minimum recommended georeferencing	position and orientation	position only
Point Density (pts/m^2)	30-250	350-5500
Point Spacing (cm)	6-20	1-5
Can penetrate dense vegetation	yes	no
Reliant on surface texture	no	yes
Reliant on lighting conditions	no	Yes
Recommended for implementing real-time processing on aircraft	yes	no

2.2. UAS Selection and Sensor Integration

An initial step in this project involved the selection of suitable remote aircraft, lidar, and direct georeferencing systems. Three basic categories of remote aircraft exist: multirotor aircraft (e.g., quadcopters, hexacopters, octocopters, etc.), fixed-wing aircraft (gliders), and helicopters. Each has specific advantages and disadvantages (Otero et al., 2015; Gillins et al., 2018), but the following broad characterization can be made: fixed-wing aircrafts are best for covering large areas efficiently on a single battery but cannot hover; multirotor aircrafts are less efficient for covering large areas but are good for hovering in place and also allow vertical takeoff and landing (VTOL); remote helicopters, which are less common, are often large, gas-powered aircraft that have greater lift capabilities. For traffic network monitoring, the ability to hover is critical, and vertical takeoff and landing are advantageous. Meanwhile, gas-powered remote helicopters, while capable of lifting greater payloads, could be considered too large, loud, and/or unwieldy to operate near roadways. Hence, multirotor aircrafts are the logical choice.

Having determined that multirotor UAS are most suitable for traffic network monitoring—and most other transportation-related applications, including bridge inspection (Gillins et al., 2018)—the next considerations involved the size and payload capabilities of the aircraft. The absolute upper limit on unmanned aircraft size is established by FAA Part 107, which requires that the maximum allowable take-off weight (includes airframe and payload) must be less than 55 lbs. to be characterized as a small UAS system (sUAS). If the maximum take-off weight is larger than 55 lbs., a different set of regulations, FAA Title 14 CFR Part 47, will govern.

Based on the aforementioned considerations and the resources available, the remote aircraft selected for use in this project was a DJI S1000 (Figure 2.1). The airframe is an octocopter weighing 4.1 kg (9 lbs.) with a maximum take-off weight (MTOW) of approximately 11 kg (24 lbs.), well below the maximum allowable weight of 55 lbs. required by Part 107. The aircraft was controlled using a DJI A2 flight controller and was unable to perform automated flights (i.e., following pre-planned flightlines and waypoints), resulting in all flights being controlled manually by the pilot on the ground. The inability to automatically navigate the remote aircraft along pre-planned flightlines adversely affected operational efficiency in this project. However, the manual flights were preferred, due to the enhanced safety, given the proximity to active roadways.

Figure 2.2.1 DJI S1000 airframe selected for this project.

Similar to the aircraft selection, the selection of a lidar system and direct georeferencing system was driven by practical considerations, including size, weight and power requirements and availability of existing equipment for use by the project team. Based on the above considerations, the selected lidar system was a Velodyne Puck LITE. The VLP-16, shown in Figure 2.2, is a compact lidar system operating at a wavelength of 905 nm, using 16 laser/detector pairs, with manufacturer-specified 100-m operating range, depending on target reflectivity at the laser wavelength (Velodyne, 2018; Glennie et al., 2016). The acquisition parameters and settings are summarized in Table 3.1. The direct georeferencing system selected was an OxTS xNAV 200 global navigation satellite system (GNSS)-aided inertial navigation system (INS), shown in Figure 2.3, with additional parameters listed in Table 3.1.

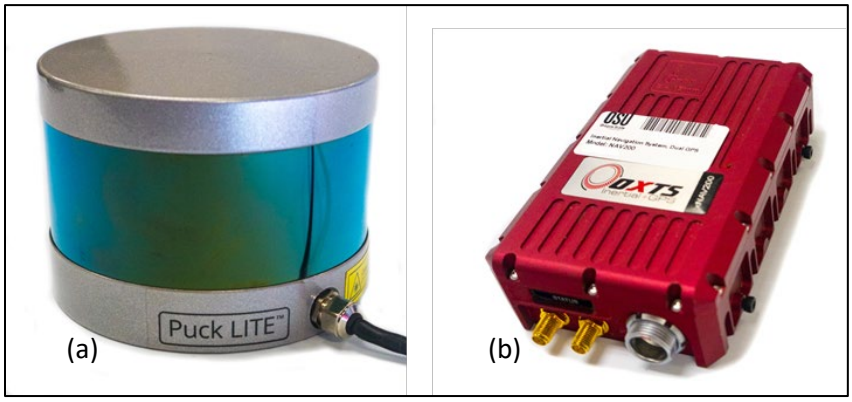

Figure 2.2.2 Final sensor payload including the VLP-16 LITE (left) and the xNAV200 inertial navigation system (right).

The next step was to integrate the lidar and direct georeferencing systems onto the UAS. To accomplish this, a custom mount was designed and 3D printed in-house. Creation of this mount in-house allowed the most flexibility for mounting to the custom DJI S1000 airframe being used and provided the project team the ability to precisely calibrate the 3D offsets ("lever arms") between the origins of the laser scanner reference frame and the INS reference frame. (The importance of these lever arms will be further discussed in the lidar point cloud generation section of this report.) After the mount was 3D printed, the VLP-16 LITE and xNAV200 GNSS-aided INS were rigidly bolted to the mount (Figure 2.3), that was then fixed to the airframe using an off-the-shelf vibration dampening adapter (Figure 2.4).

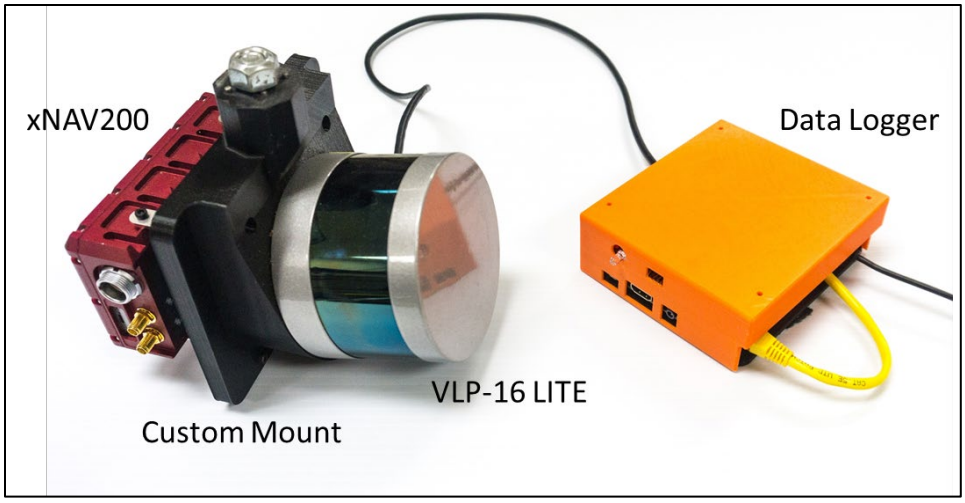

Figure 2.2.3 Final sensor payload including xNAV200 rigidly fixed to the custom mount (left) and the data-logger for the VLP-16 LITE (right).

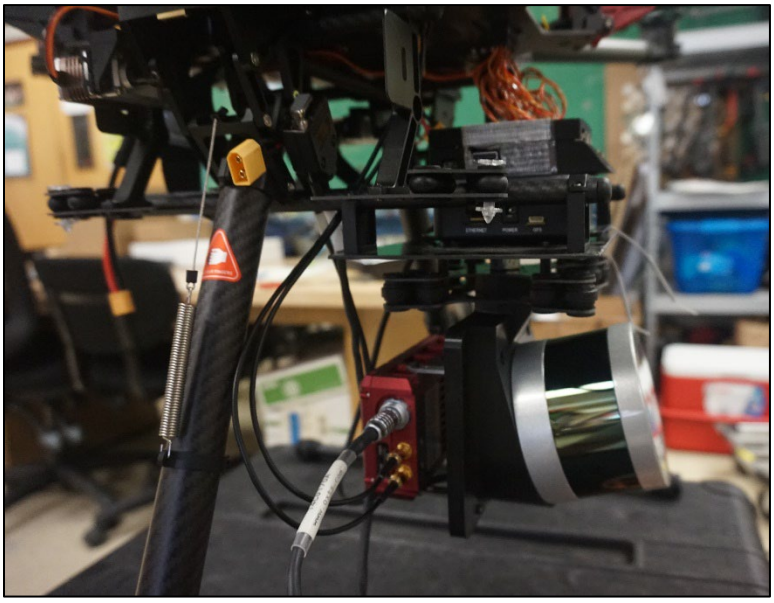

Figure 2.2.4 Final sensor payload loosely fixed (via the vibration-dampening adapter, seen just above the lidar) to the DJI S1000 airframe.

Table 2.2 Summary of mapping system components

Component	**Make/model**
UAS	DJI S1000
lidar	Velodyne Puck Lite 16
Direct georeferencing system	OxTS xNAV 200

2.3. Lidar Point Cloud Generation and Testing

After the system integration was completed, custom software was written to perform the georeferencing of the lidar data, as the original output consists of a raw, unprocessed, flight trajectory collected by the GNSS-aided INS and raw lidar data with reference frame of the lidar data being in the scanner's own coordinate system (SOCS). The workflow implemented to create the georeferenced point cloud is illustrated in Figure 2.5. The general steps in this workflow are common to most airborne lidar systems (e.g., Petrie and Toth, 2009). The basic requirements include post-processing the aircraft trajectory and combining it with the raw lidar data in conjunction with the measured leaver arms previously mentioned in Section 2.2 using a form of the geolocation equation. It is important to note that the georeferencing can be performed in real time, although the highest accuracy results require post-processing.

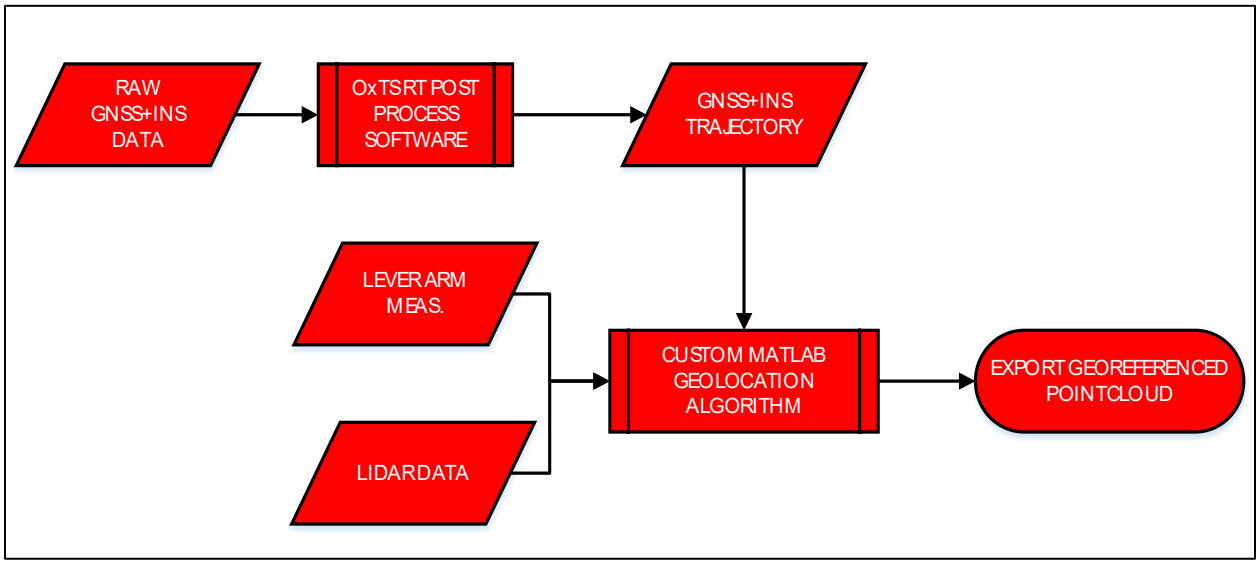

Figure 2.2.5 Workflow used to georeference lidar data.

An overview of how the laser geolocation equation is used to convert the raw lidar data from SOCS reference frame to the conventional reference frame (e.g., Universal Transverse Mercator or U.S. State Plane coordinate systems) is depicted in Figure 2.6 and is summarized below.

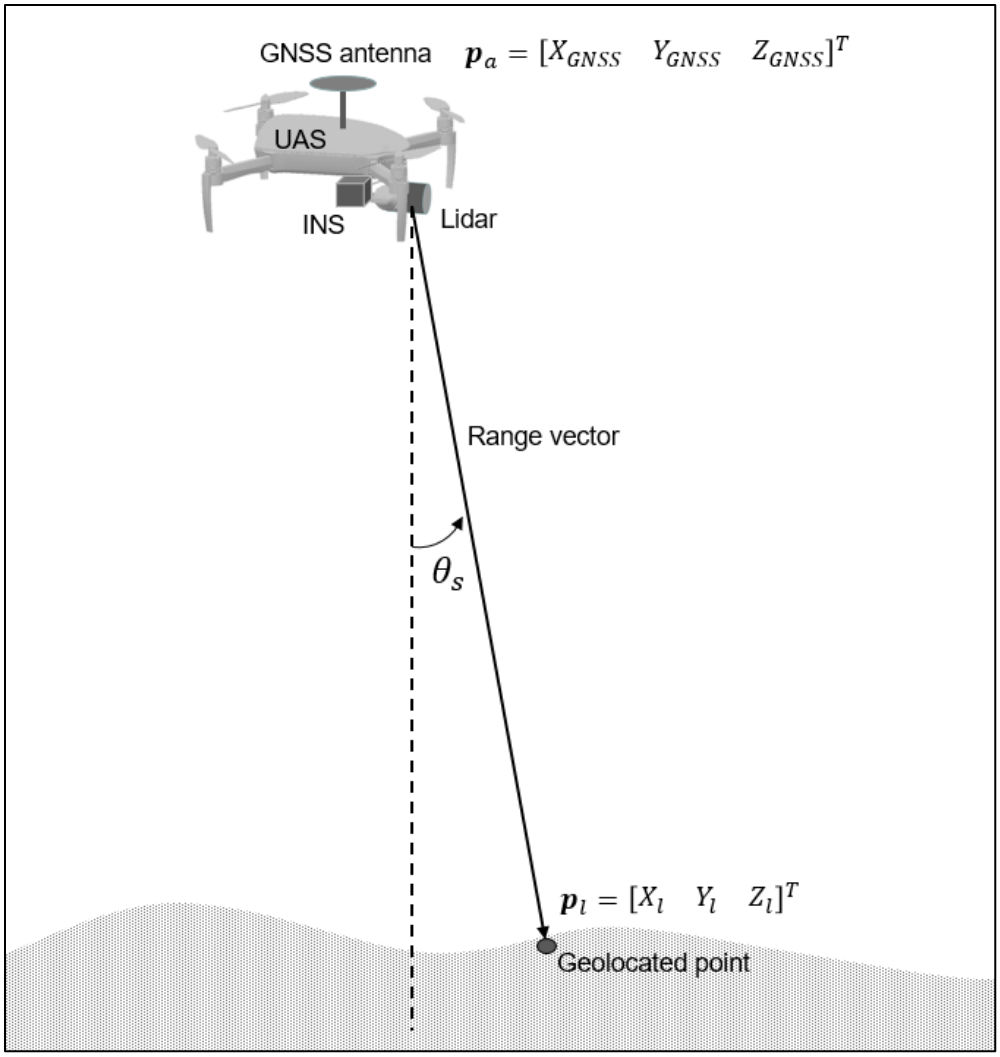

Figure 2.2.6 Laser geolocation.

The laser geolocation (i.e., the georeferencing of lidar returns to compute 3D spatial coordinates, relative to the mapping frame, of each point) is achieved using the following equation:

$$\boldsymbol{p}_l = \begin{bmatrix} X_l \\ Y_l \\ Z_l \end{bmatrix} = \begin{bmatrix} X_{GNSS} \\ Y_{GNSS} \\ Z_{GNSS} \end{bmatrix} + \boldsymbol{R}_{ll}^{m} \boldsymbol{R}_{b}^{ll} \left(\begin{bmatrix} \delta x \\ \delta y \\ \delta z \end{bmatrix} + \boldsymbol{R}_{ls}^{b} \begin{bmatrix} 0 \\ 0 \\ -\rho \end{bmatrix} \right) \quad (1)$$

Where ρ is the range (equal to half the round trip travel time of the laser pulse times the speed of light in the atmosphere); $\boldsymbol{R}_{ls}^{b}$ rotates the range vector from the laser-scanner (*ls*) frame to the UAS body (*b*) frame using the measured scan angle, θ_s; $[\delta x \quad \delta y \quad \delta z]^T$ is the vector expressing the GNSS-antenna-to-UAS-body frame offset or "lever arm"; $\boldsymbol{R}_{b}^{ll}$ rotates from the body frame to the local level (e.g., North-East-Up) frame; $\boldsymbol{R}_{ll}^{m}$ rotates from the local level frame to the mapping frame (e.g., Universal Transverse Mercator coordinate systems), and $[X_{GNSS} \quad Y_{GNSS} \quad Z_{GNSS}]^T$ is the position of the UAS's GNSS antenna. The rotation matrices in Equation 1 are generally standard and well known within the Geomatics

community (e.g., Filin, 2003; Grewel et al., 2013; El-Sheimy, 2017; Eren et al., 2019). The rotation from the body frame to the local level frame is achieved using the roll (Φ), pitch (Θ), and heading (Ψ) from the INS:

$$\boldsymbol{R}_b^{ll} = \begin{bmatrix} \cos\Theta\sin\Psi & -\cos\Psi\cos\Phi - \sin\Psi\sin\Theta\sin\Phi & \cos\Psi\sin\Phi - \sin\Psi\sin\Theta\cos\Phi \\ \cos\Theta\cos\Psi & \sin\Psi\cos\Phi - \cos\Psi\sin\Theta\sin\Phi & -\sin\Psi\sin\Phi - \cos\Psi\sin\Theta\cos\Phi \\ \sin\Theta & \cos\Theta\sin\Phi & \cos\Theta\cos\Phi \end{bmatrix} \quad (2)$$

Failure to properly apply the laser geolocation equation can be one of many issues that may lead to a poorly georeferenced point cloud. Large errors can be caused by having a poor trajectory accuracy that might, in turn, be due to an extended period of loss of lock on GNSS satellites. Biases and other forms of systematic error may also be due to incorrectly measuring the lever arms, or improperly calibrate the lidar system. If relative biases, meaning a bias relative to points within the same dataset (see, e.g., Figure 2.7), are present in the data, they can become problematic when attempting to extract features using machine-learning algorithms.

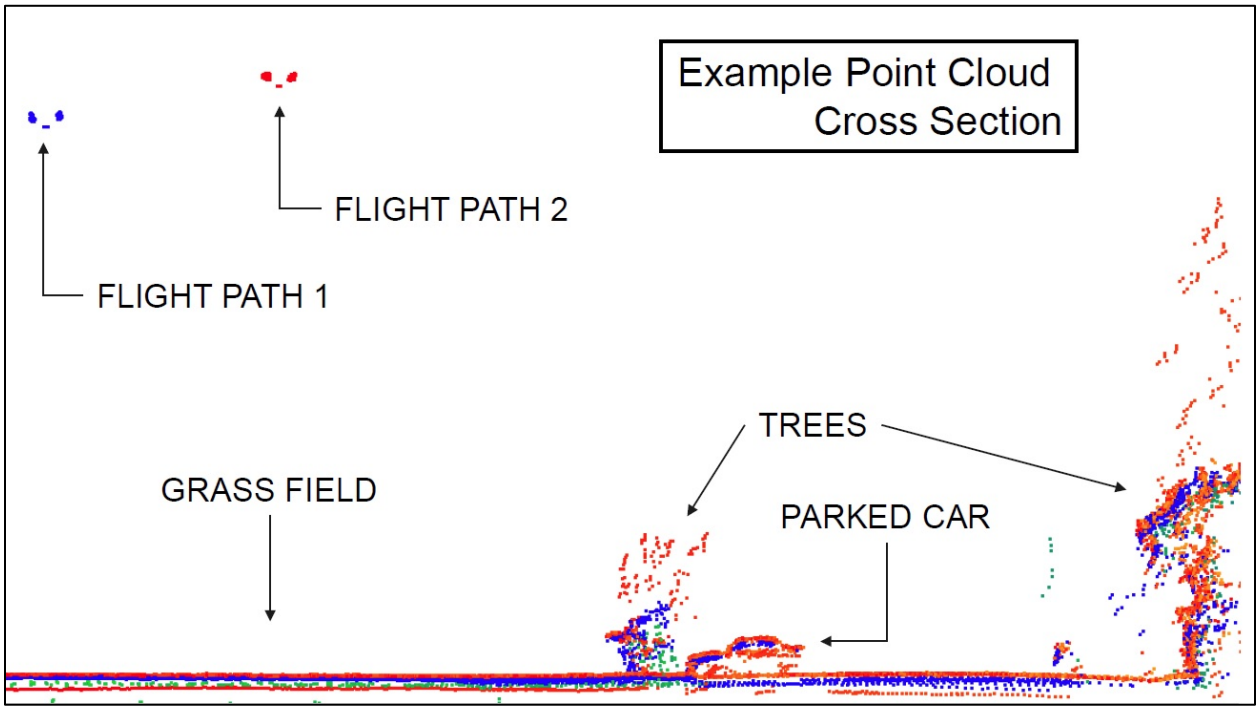

Figure 2.2.7 Illustration of the need for accurate georeferencing. Here, a slight offset (bias) between the points from flight paths 1 and 2 (shown in blue and red, respectively) is evident. If uncorrected, this offset could pose challenges for the machine learning algorithms used to auto-extract features.

The UAS lidar data were fed into an end-to-end analytics system, developed by the University of Idaho (UI) project team members, responsible for reading directly from the raw lidar system output, performing georeferencing (as described above), creating the convolution scan environment, and detecting vehicles. The team also created a pipelining process to sequentially scan each batch of collected data during any interval, while the next batch is being collected, thus mimicking the exact processing that would occur onboard the UAS. This new system was tested using different computing

capabilities (different processors with differing RAM), and different time resolutions for running the algorithm on the entire scan. For each of the time resolutions and each stage of the code, runtime was recorded, along with the detection accuracy, and the number of false alarms. The details of the design and implementation of this system are illustrated in Chapter 4.

CHAPTER 3. UAS-LIDAR DATA COLLECTION AND EVALUATION

The first test dataset was acquired at a Newberg-Dundee bypass construction site in collaboration with the Oregon Department of Transportation (ODOT). This section of the bypass was, at the time, recently completed but remained closed off to the public, allowing the UAS to be flown directly over the roadway. The goal of this data acquisition was to collect a dataset with multiple transportation features in the scene that the project team could use to begin developing the feature extraction algorithms. Some of the features acquired at this site included: signs, vehicles, pavement markings, and guardrails. In addition to collecting data of roadway features, the project team also conducted flights over stationary vehicles and a participating moving vehicle. Analysis of the data revealed the effects of incidence angles (due to the super-elevated roadway) and the freshly paved (very dark) pavement had on signal return dropouts. (Note: a “dropout” is defined as a transmitted lidar pulse for which no detectable return signal is received.) As a result of these site characteristics, the project team had to decrease the flying altitude over the roadway from 40 m (130 ft) down to 30 m (100 ft) and modify the trajectory to increase the total point returns. From analysis of the data, an even lower flying height would have be beneficial for reducing the number of dropouts.

Figure 3.1 UAS data collection at the Newberg Dundee construction site.

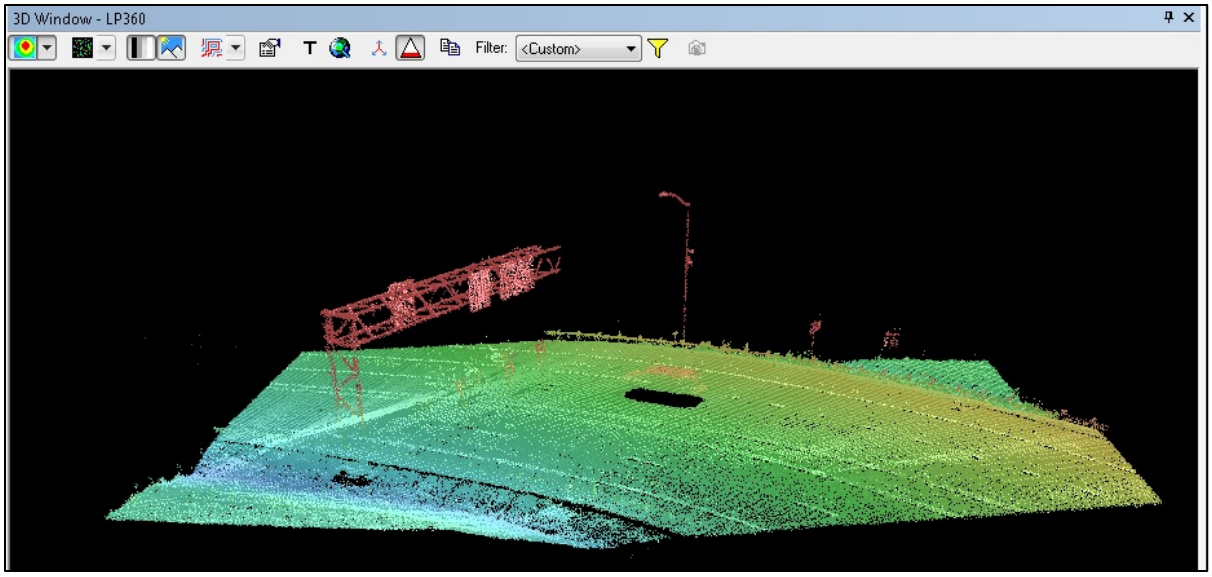

Figure 3.2 Georeferenced lidar point cloud for Newberg-Dundee site.

The second UAS-based lidar data set was collected over a portion of the Oregon State University (OSU) campus, including a parking lot with several parked vehicles, on April 17, 2018. All project team members from both OSU and UI participated in the data collection (Figure 3.3). The lidar data sets were subsequently used by UI project team members in developing and testing the vehicle-detection algorithms.

Figure 3.3 Data collection on OSU campus.

The acquisition parameters and system settings for the first two UAS-lidar data acquisitions are listed in Table 3.1. Lidar system parameters were obtained from Velodyne (2018) and Glennie et al. (2016).

Table 3.1 UAS-lidar data collection parameters and acquisition settings.

Parameter	**Acquisition setting**
Lidar system	Velodyne VLP-16
Laser wavelength	903 nm
Laser safety class	Class 1
Lidar horizontal field of view	360°
Lidar vertical field of view	30°
Angular resolution	2° vertical, 0.1-0.4° horizontal
Laser/detector pairs	16
Max lidar measurement rate	300 kHz
Laser pulse width	6 ns
Max output energy	0.19 µJ
Nominal ranging accuracy	±3 cm
Nominal lidar power consumption	8 W
Power requirement	10-31 V
Lidar physical dimensions	10.3 cm diameter; 7.2 cm height
Inertial navigation system (INS)	OxTS xNAV200
INS measurement rate	100 Hz
Nominal INS accuracy	Roll and pitch: 0.05°; Heading: 0.15° (1σ)
Nominal INS power consumption	6.5 W
Airframe	DJI s1000
Max flight altitude	120 m (400 ft), AGL

A third lidar data set was collected on August 16, 2018. The goal of this data acquisition was to simulate lidar data collected by a stationary (hovering) UAS scanning an intersection. The Velodyne VLP-16 lidar system (described earlier) and a video camera were fixed-mounted to a railing overlooking the Monroe-14th Street intersection in Corvallis, Oregon (Figure 3.4). These sensors were used to collect 20 minutes of data from three different orientations: 1) scanner oriented horizontal with main axis pointing across the intersection; 2) scanner oriented vertical with main axis pointing across the intersection; and 3) scanner oriented vertical with main axis pointing across Monroe Street only. Analysis of the data revealed that vehicles were well detected and could be readily tracked in the lidar scans.

Figure 3.4 Stationary lidar data acquisition overlooking intersection.

The fourth and final data collection for this project utilized a different aircraft and lidar system. Data were collected with a Phoenix Lidar Systems MiniRanger (Figure 3.5), incorporating a Riegl miniVUX-1UAV lidar and an INS using fiber optic gyroscopes (FOGs), for a section of roadway near the University of Washington campus on November 27, 2018. The MiniRanger operates at a wavelength of 905 nm, with a maximum effective measurement rate of 100 kHz, and nominal ranging accuracy of 1.5 cm (Kellner et al., 2019; Phoenix LiDAR Systems, 2019). A benefit to this lidar system was the increased ranging distance of 250 meters (at 60% target reflectivity), as compared to the VLP-16 LITE, which had a nominal maximum range of 100 meters. Through the oblique scanning angle and increase in ranging distance (as compared with the other UAS lidar system used in this study), this platform enabled the flights to be completed at a greater distance from the roadway while still maintaining an acceptably small number of dropouts. The operational lessons-learned from all four field data collection efforts undertaken in this project were compiled and are presented in Chapter 5 of this report.

Figure 3.5 Phoenix Lidar Systems MiniRanger, incorporating a Riegl miniVUX-1UAV lidar.

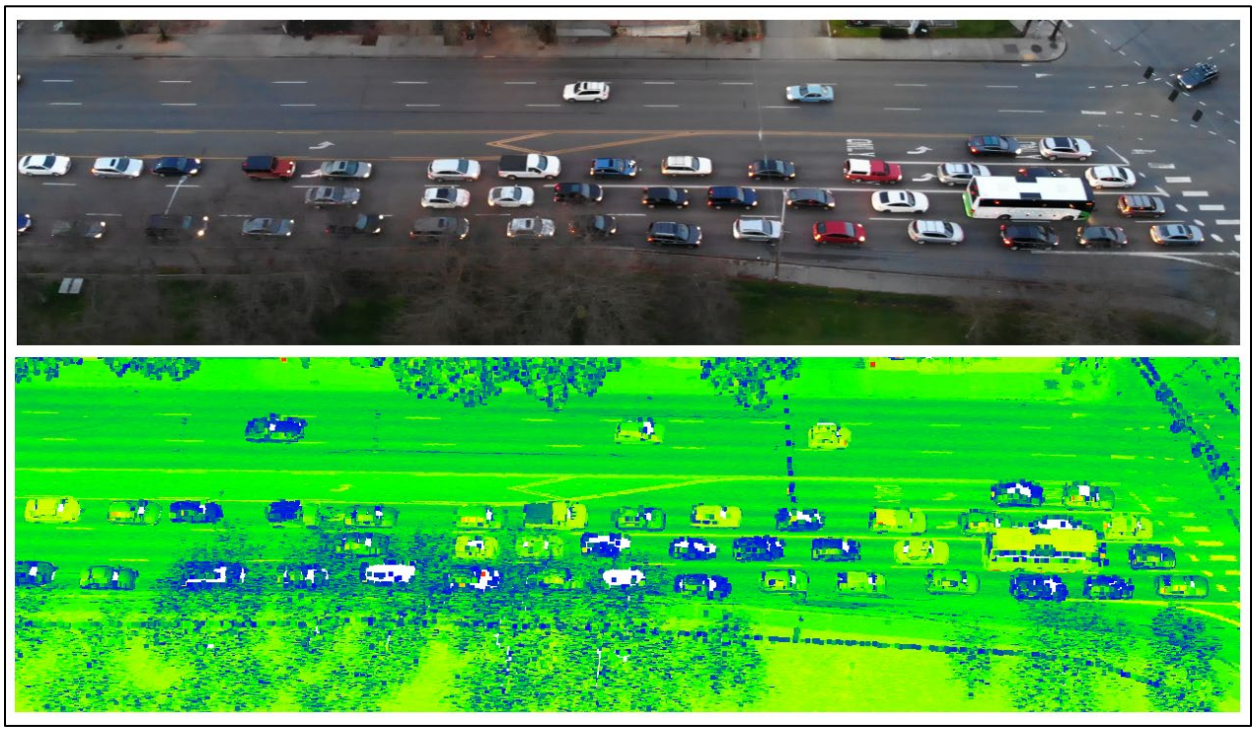

Figure 3.6 lidar data, colored by return intensity (bottom) with a snap shot of the co-acquired RGB video (top) collected at an intersection on UW campus.

Figure 3.7 Lidar UAS acquisition using Phoenix Lidar Systems MiniRanger.

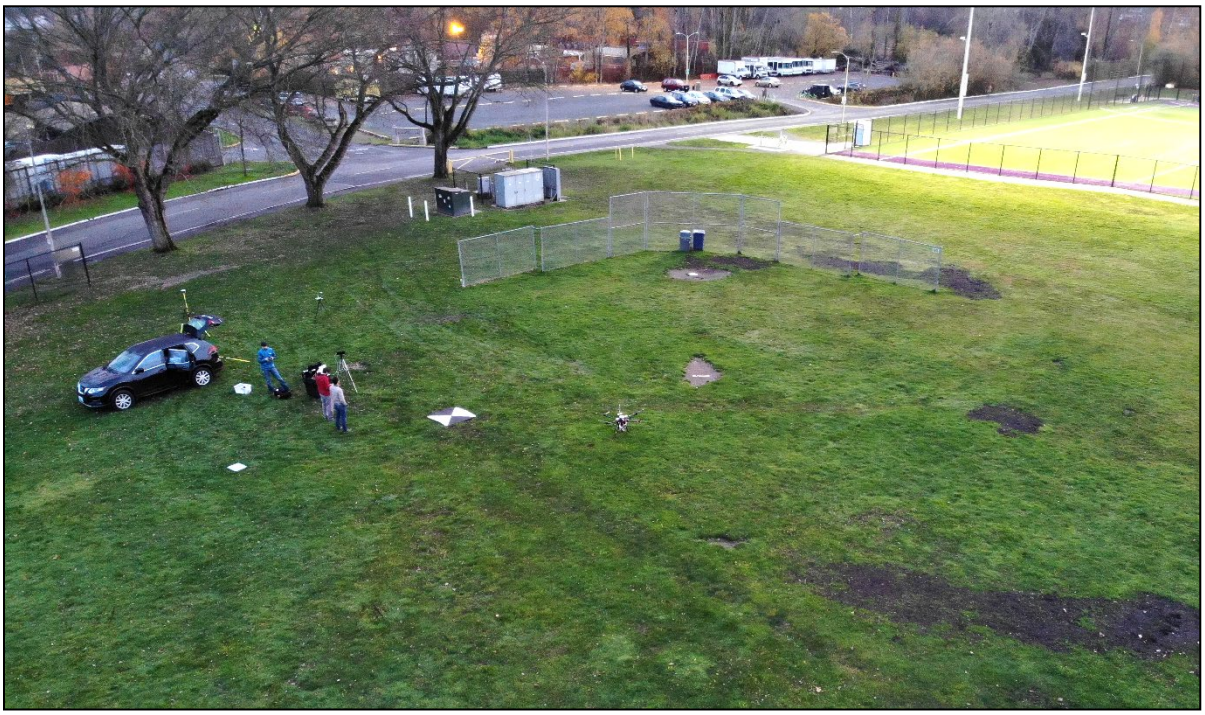

Figure 3.8 Field operations for UAS lidar acquisition.

CHAPTER 4. DESIGN AND IMPLEMENTATION OF MACHINE LEARNING ALGORITHMS

The aim of this portion of the project was to develop an end-to-end vehicle recognition program (all built in C++) from lidar point clouds in real-time and on-board the UAS. As described earlier, the system for the real-time airborne traffic monitoring is composed of a UAS, a lidar scanner, a global navigation satellite system (GNSS) receiver, an inertial navigation system (INS), and an on-board computer. With the use of such equipment, we can divide the operation of the system into two time dependent blocks: a) scanning, and b) data analysis. Given that the data collection by the lidar scanner and positioning system can be operated alongside other computations within the on-board computer, the data analysis block is designed to run in parallel with the scanning block. Therefore, it is essential to select a scanning block time that allows the data processing algorithm to perform the computations before the next scanning block starts, as shown Figure 4.1. While the lidar and positioning systems scan the data for a given block, the on-board computer is processing the data from the previous block and needs to finish its computations before the end of the current scanning block. In this way, we can ensure that the rate of data accumulation does not exceed the capability of the system to process the information.

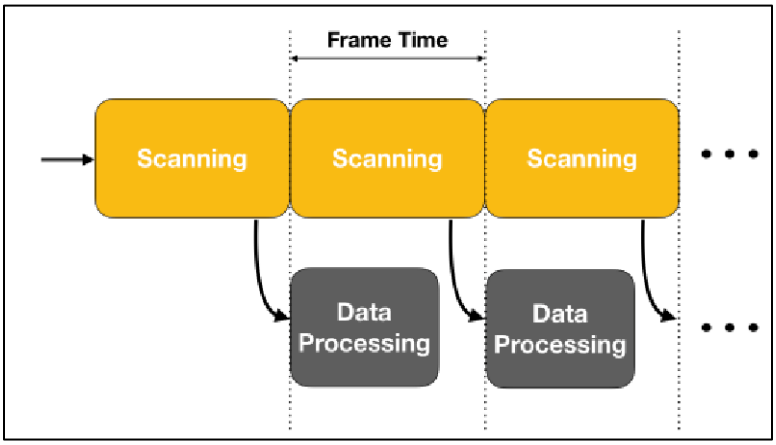

Figure 4.1 Scheduling of scanning and data processing blocks for the airborne lidar based vehicle recognition system.

With the information collected during the scanning block, the data analysis algorithm combines all of the available data to create a 3D representation of the environment, referenced to the UAS's position during the flight. This 3D space goes through a filtering step to select the data within the range of interest and then it undergoes a convolutional step for the vehicle detection. The algorithm steps are further explained below.

Step 1: Read and Prepare Data

At the beginning of the data processing block, the on-board computer requests the lidar and UAS positioning data for the most recent frame and performs the initial data preparation. The raw lidar data is presented with the time of flight (TOF) distance, along with a vertical and horizontal firing angles, ω and α, respectively. In order to reconstruct the 3D distance from the lidar, the TOF distances are decomposed in *X*, *Y*, and *Z* components based on the firing angles, as shown in Figure

4.2. Since a time stamp is not assigned to all data points, the periodicity of the beam firings is used to assign a timestamp to the remaining points. The positioning information comes with the time stamp for each measurement with (a) Latitude, (b) Longitude, (c) Altitude, (d) Heading, (e) Pitch, and (f) Roll. The geodetic coordinates (latitude and longitude) are then converted to Universal Transverse Mercator (UTM) northings and eastings, due to the computational ease of working with projected coordinates. The coordinate computations are as follows (Velodyne, 2018)

$$X = R \cos \omega \sin \alpha \tag{3}$$

$$Y = R \cos \omega \cos \alpha \tag{4}$$

$$Z = R \sin \omega \tag{5}$$

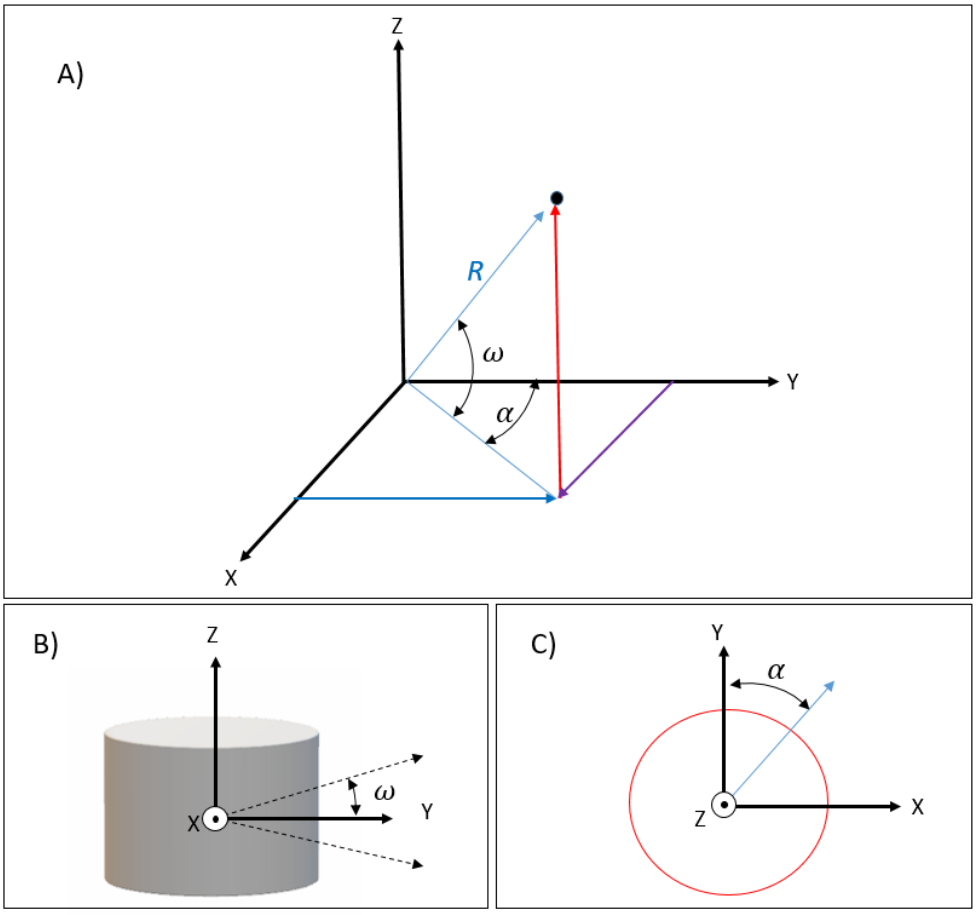

Figure 4.2 A) coordinate decomposition for Velodyne VLP-16, based on TOF distance, *R*, and angles, ω and α; B) side view; and C) top view (adapted from Velodyne, 2018).

Step 2: Perform Coordinate Transformations

The laser scanner and positioning system each collect data relative to their own 3D coordinate system. A 3D conformal transformation, consisting of rotations about three axes and translations to align the origins of the respective frames is performed to bring the data into a common frame. This step makes use of the lever arms that were previously described, and the measured attitude data, in the form of Tait-Bryan angles (roll, pitch, and heading).

Step 3: Interpolate Data

Given that the measurement rate of the INS unit on the UAS is much lower than the lidar system's pulse repetition rate, the UAS trajectory data (position and orientation at each epoch) needs to be interpolated to provide an appropriate origination coordinate for each beam firing. Before the data sets with the position of the UAS and lidar-measured distance can be combined, a position needs to be assigned to the origin of each laser pulse. Given that the INS measurement rate is 100 Hz, a linear interpolation can be used to calculate the UAS position between two measurements.

$UAS_1 \setminus\setminus (data_1, t_1)$
$UAS_2 \setminus\setminus (data_2, t_2)$
$LiDAR_k \setminus\setminus (lidar_1, t_{lidar})$

if $t_1 \leq t_{lidar} \leq t_2$ **then**

$$data_k = data_1 + (data_2 - data_1) \cdot \frac{t_{lidar} - t_1}{t_2 - t_1}$$

end

Algorithm 1: Linear Interpolation

Figure 4.2 Algorithm for interpolation of UAS trajectory, based on differing data rates of INS and lidar measurement.

Step 4: Apply Geolocation

With all the lidar coordinates properly referenced to the UAS frame, the two data sets can be combined once axial rotations (heading, pitch, and roll) corrections have been applied. During the flight, changes in direction and speed cause the UAS to experience rotations as it corrects its course. The equations below demonstrate how the final data set can be obtained from the UAS position, lidar TOF distance measurements, and axial rotation corrections.

$$R_z(h) = \begin{bmatrix} \cos(h) & -\sin h & 0 \\ \sin(h) & \cos(h) & 0 \\ 0 & 0 & 1 \end{bmatrix} \quad (6)$$

$$R_y(p) = \begin{bmatrix} \cos(p) & 0 & \sin p \\ 0 & 1 & 0 \\ -\sin(p) & 0 & \cos(p) \end{bmatrix} \quad (7)$$

$$R_x(r) = \begin{bmatrix} 1 & 0 & 0 \\ 0 & \cos(r) & -\sin(r) \\ 0 & \sin(r) & \cos(r) \end{bmatrix} \quad (8)$$

$$R(h, p, r) = R_z(h) R_y(p) R_x(r) \quad (9)$$

$$\begin{bmatrix} X \\ Y \\ Z \end{bmatrix}_{Final} = R(h, p, r) \begin{bmatrix} X \\ Y \\ Z \end{bmatrix}_{LiDAR} + \begin{bmatrix} X \\ Y \\ Z \end{bmatrix}_{UAS} \quad (10)$$

Step 5: Data Optimization

After the proper 3D referencing calculations, the final point cloud needs to be optimized for the convolution calculations, the most computationally expensive step of the algorithm. First, repeated points need to be removed from the data set. This step is necessary because the lidar scanner can detect the same location of the area scanned during different parts of the flight, yielding the same *X*, *Y*, and *Z* coordinates after the referencing calculations. Once the unique point cloud is obtained, the road data set can is trimmed for the limits of the road segment of interest. Since the proposed system is meant to work with scheduled flights, the road limits can be obtained from the scheduled flight trajectory. Next, the point cloud needs to be filtered for the road level of interest, which can be based on the minimum data *Z* coordinate on the frame. The algorithm can concentrate in regions that vehicles are likely to occupy. The last optimization in this step is to add an offset to the data so it can start at the origin of the 3D Cartesian coordinates and continue along the positive axes.

Step 6: Convolutional Recognition

The final step of the vehicle-identifying algorithm is to perform the convolution computation. Utilizing a pre-selected reference vehicle filter (shown in Figure 4.3), the processed data captured by the system is convolved with this vehicle model to find similarities with the scanned data. Based on a selected threshold for the result of the convolution computation, the algorithm determines whether a vehicle is located in a given location. Since the calculations near an actual vehicle may yield multiple convolution results that surpass the chosen threshold, due to partial superposition between the actual vehicle and the model, smaller convolution results near a higher value need to be disregarded. In other words, a scanned vehicle will have partial matches with the selected model, and these partial matches need to be filtered from the desired “full” match between the point clouds. At the end of the data processing block, the algorithm outputs the coordinates for the detected vehicles minus the offset it had generated while optimizing the data. The performance of

the algorithm described above can be fine-tuned, based on the scanned time for each frame, the resolution step for the convolution computation, and the convolution result threshold.

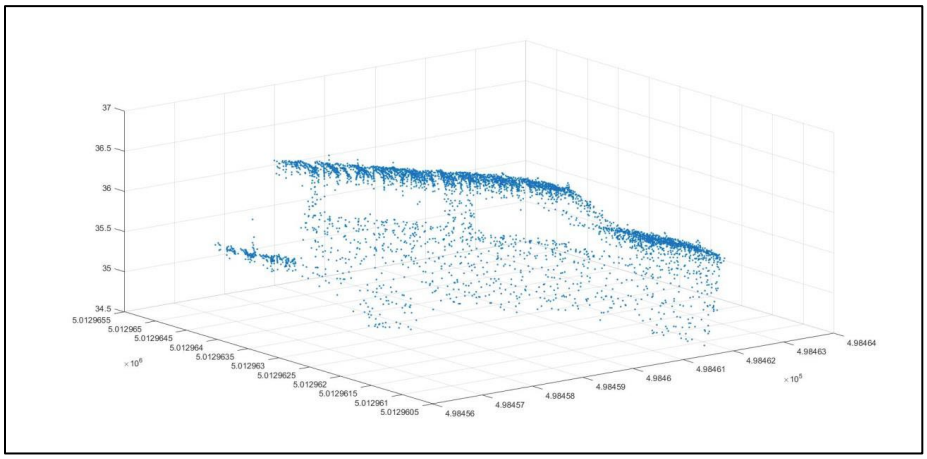

Figure 4.3 Reference vehicle filter.

CHAPTER 5. RESULTS

5.1. UAS Operations

One key result of this project is a set of guidelines or best practices for operational use of UAS for traffic network monitoring. Overarching guidelines for UAS for transportation applications are listed in the PacTrans *UAS in Transportation Expo* final report, stemming from a PacTrans "Success Stories" project (Parrish et al, 2018) aimed at disseminating the results of this project and previous UAS research in support of the Pacific Northwest Transportation Consortium. Key recommendations are summarized below:

- Due to the rapidly evolving technological and regulatory aspects of UAS, state transportation agencies seeking to use UAS operationally are advised to develop a formal UAS program, with a defined structure and roles and responsibilities.
- Standard operating procedures (SOPs) should be developed for as many operational aspects of the program as possible, as SOPs help reduce on-the-fly decision-making in stressful field situations.
- For operations in controlled airspace, it is important to initiate correspondence with Air Traffic Control (ATC) as early as possible in the project planning stage. Likewise, conversations with landowners should occur as early as possible.
- The FAA Low Altitude Authorization and Notification Capability (LAANC) is a very useful utility, which automates the application and approval process for airspace authorizations, enabling UAS pilots to obtain access to controlled airspace at or below 400 ft.
- When the flight crew and flight operations are visible to passing motorists, the flight crew should be as conspicuous and official as possible, including wearing safety vests, headsets, and other personal protective equipment, as required.
- UAS firmware updates should be avoided in the field; firmware should be updated and tested in a non-operational environment away from traffic.

Additionally, the following operational recommendations and lessons-learned are specific to UAS traffic network monitoring and the operations performed in this research:

- Low-reflectance (i.e., dark) surfaces, such as new asphalt, result in a significant number of lidar "dropouts" (i.e., non-detections, leading to data gaps). This situation is exacerbated when combined with large inflection angles (i.e., when scanning obliquely to the roadway to maintain the required stand-off distance). While flying lower to reduce laser range would seem to be a logical solution, this typically cannot be done for the safety reasons noted below. Hence, it is critical to ensure that the lidar system used has sufficient range to detect returns from low-reflectance surfaces at the required operational ranges.
- In addition to maintaining adequate distance from drivers to minimize potential driver distraction (Hurwitz et al., 2018; Barlow et al., 2019a; Barlow et al., 2019b), adequate flying altitude must be maintained to minimize impact to pedestrians, while still receiving adequate point returns. (While FAA Part 107 prohibits flights over non-participants, a more stringent requirement of ensuring UAS operations are unnoticed by pedestrians is recommend, to the extent feasible.)
- Moving vehicles can appear distorted in the resulting point cloud

- When flying against the moving flow of traffic, vehicles appear compressed in the point clouds, whereas flying with the flow of traffic, vehicles appear elongated (streaking effect).
- In some areas, it can be difficult or impossible to calibrate the GNSS-aided INS without overflying a roadway; therefore, not all areas are suitable for being monitored under current laws and policies that preclude flights over roadways and over nonparticipants.
    - INS systems require calibration flights to warm up the INS about all axes. Requiring the user to fly "figure eights" prior to acquiring any data. This could possibly be alleviated through different methods for point cloud registrations such as any of the various SLAM based approaches.
- Lidar scanning angle/trajectory orientation has a large impact on the ability to capture specific vertical features adequately. Having a large forward/back scan angle can help alleviate this issue and thus possibly eliminate the need for multiple flight lines.
- A geo-fence should be used to assist in ensuring that the aircraft does not at any time fly over the roadway and any areas containing nonparticipants.

5.2. Vehicle Detection

The performance evaluation of the system/algorithm was conducted in a controlled environment, emulating real-time conditions and allowing for the assessment of different processing units. During the tests, the computer received the raw data obtained from the lidar scanner and positioning devices (replicating a real-time data stream) and provided the locations of vehicles according to the computations in the algorithm described above. For this evaluation, two airborne UAS scans were utilized with different values for the performance variables, frame time, convolution threshold, and resolution step. For the end-to-end tests, from data collection to vehicle identification, two processors were utilized to obtain the time required for the data processing block. The first processor, a 3GHz Intel Core 2 Duo, was tested with 2GB, 4GB, 8GB of RAM while the second processor, a 2.5GHz Intel Core i7, had a fixed 16GB DDR3 of RAM.

The first data set corresponds to the scan of a free road segment containing a single moving vehicle. Figure 5.1 (a) displays the post-processing point cloud with the vehicle circled in red. The second data set scanned an urban setting with multiple vehicles in a parking lot. Figure 5.1 (b) displays the post-processing point cloud with some of the visible vehicles circled in red. In addition to vehicles, the figure also displays buildings and trees, which help test the algorithm in the typical environment in which the airborne lidar based system will be utilized.

Analysis of the algorithm applied to the two datasets demonstrates that the proposed system can be utilized with moving and static vehicles. The point clouds shown in Figure 5.1 were utilized for a visual verification of the algorithm. For this analysis, the vehicle model utilized for the convolution step was extracted from the point cloud. During the initial steps of the development of the algorithm, the post-processing point cloud for the single vehicle was subdivided into frames of different lengths and evaluated for different convolution step resolutions.

Table 5.1 displays the time required to identify the single vehicle with a resolution of 0.1 and 1 meters. The X Range variable serves as an illustration to the quantity of data points in the scanned area, helping

to demonstrate that the difference in timing for smaller resolutions increases considerably as the number of points in the data set grows.

Table 5.1 Single Vehicle Convolution Timing.

X Range (m)	10		20		50		100	
Resolution (m)	0.1	1	0.1	1	0.1	1	0.1	1
Convolution Step (msec)	578.983	10.419	2425.551	17.438	9052.797	42.436	18444.752	57.874

Analyzing the data set with multiple vehicles and other urban features provides a better understanding on how the convolution threshold and the time interval selected for a frame affect the Detection Ratio and False Detection Ratio of the algorithm. The data packets from the raw data set for the multiple vehicle scanned environment was segmented into different time frame lengths from 1 second to the full length of the data set, 47 seconds. The graphs in Figure 5.1 display the Detection Ratio and False Detection Ratio for convolution thresholds of 100, 150, 200, and 250, computed as follows:

$$\text{Detection Ratio} = \frac{\#\ \text{Correctly Detected Vehicles}}{\#\ \text{Actual Vehicles}} \cdot 100\% \tag{11}$$

$$\text{False Detection Ratio} = \frac{\#\ \text{Falsely Detected Vehicles}}{\#\ \text{Total Detected Vehicles}} \cdot 100\% \tag{12}$$

Tables 5.2 to 5.5 present the average time for the different frame times and convolution thresholds considered with different amounts of RAM. Under the current algorithm and systems utilized, the time requirements for the frame times considered followed Figure 4.1, maintaining the Data Processing Block timing less than the Frame Time.

The four configurations of RAM for the system present a similar timing behavior when considering the convolution threshold. While the algorithm timings for thresholds of 150, 200, and 250 are very similar for the four test scenarios, the lower threshold of 100 presents a higher time difference. This indicates that the algorithm is detecting a higher rate of partial objects, requiring more filtering computations to be performed.

In addition, the amount of RAM utilized in the testing does not seem to have a significant effect compared to that of the processor utilized. The 2GB, 4GB, and 8GB RAM configurations present very similar timing results, indicating the smaller on-board computers with lower power consumption can be selected. Moreover, it is interesting to notice that as the convolution threshold increases, the total data processing time for a frame decreases. This is due the fact that less partial matches between a scanned vehicle and the vehicle model surpass the convolution threshold, lowering the computation load.

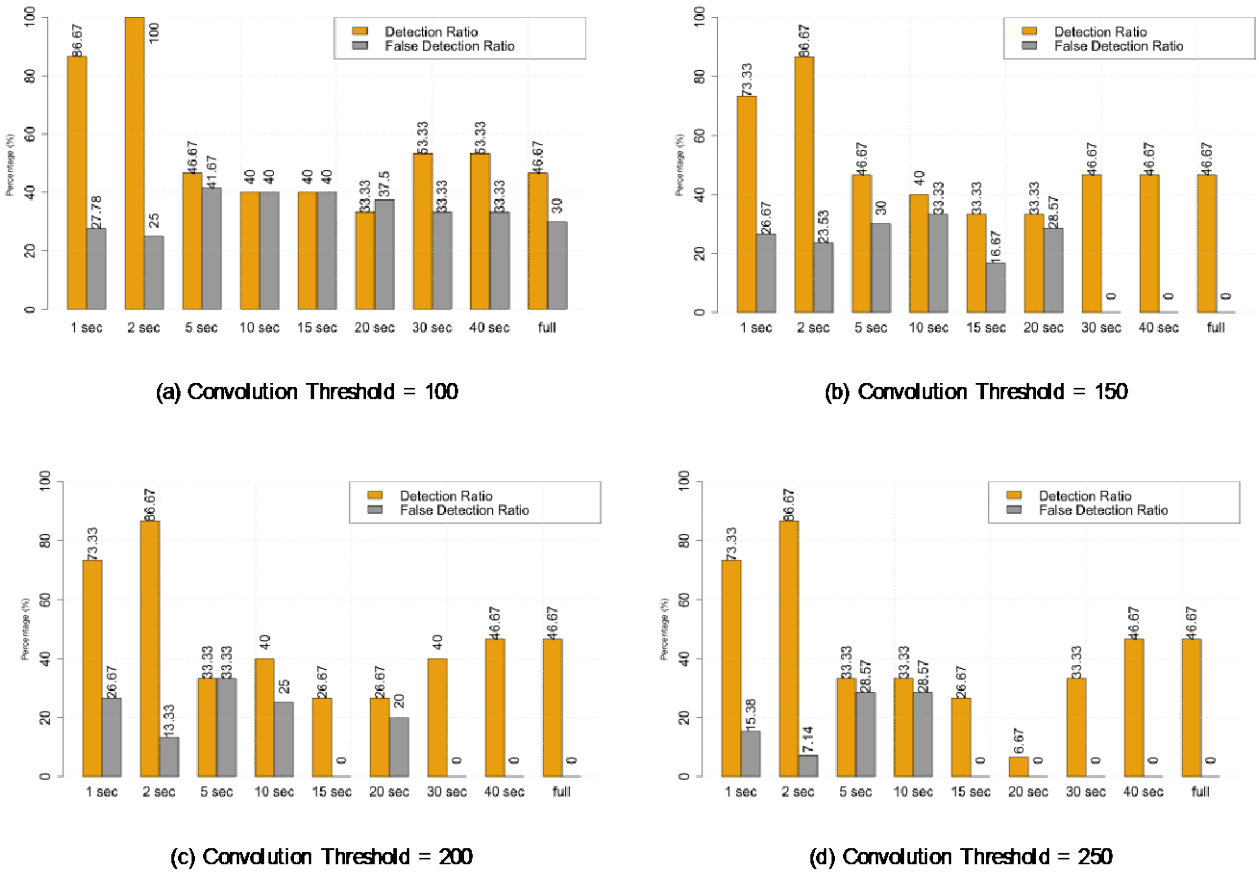

Figure 5.1 Detection Ratio and False Detection Ratio for Different Resolution Thresholds and Time Frame Segments.

Table 5.2 Average data processing time (sec) for different frame lengths and convolution thresholds for a 3GHz Intel Core 2 Duo processor with 2GB of RAM.

	Convolution Threshold	1 sec	2 sec	5 sec	10 sec	15 sec	20 sec	30 sec	40 sec	full scan (47 sec)
2 GB	100	0.544	0.729	1.296	2.632	3.754	4.974	7.228	13.540	15.780
	150	0.404	0.600	1.216	2.506	3.593	4.823	7.137	12.486	13.862
	200	0.364	0.577	1.207	2.491	3.565	4.825	7.136	12.213	13.455
	250	0.358	0.563	1.201	2.497	3.568	4.817	7.179	12.185	13.380

Table 5.3 Average data processing time (sec) for different frame lengths and convolution thresholds for a 3GHz Intel Core 2 Duo processor with 4GB of RAM.

	Convolution Threshold	1 sec	2 sec	5 sec	10 sec	15 sec	20 sec	30 sec	40 sec	full scan (47 sec)
4 GB	100	0.544	0.728	1.327	2.634	3.752	4.987	7.225	13.281	16.001
	150	0.402	0.6	1.221	2.516	3.584	4.859	7.163	12.398	13.8
	200	0.363	0.577	1.207	2.528	3.563	4.88	7.123	12.168	13.404
	250	0.356	0.563	1.209	2.497	3.582	4.841	7.12	12.234	13.31

Table 5.4 Average data processing time (sec) for different frame lengths and convolution thresholds for a 3GHz Intel Core 2 Duo processor with 8GB of RAM.

	Convolution Threshold	1 sec	2 sec	5 sec	10 sec	15 sec	20 sec	30 sec	40 sec	full scan (47 sec)
8 GB	100	0.542	0.727	1.293	2.62	3.735	4.954	7.121	13.162	15.736
	150	0.402	0.595	1.231	2.495	3.572	4.834	7.106	12.384	13.685
	200	0.363	0.57	1.197	2.482	3.566	4.773	7.179	12.175	13.345
	250	0.357	0.567	1.203	2.489	3.576	4.798	7.072	12.123	13.345

Table 5.5 Average data processing time (sec) for different frame lengths and convolution thresholds for a 2.5GHz Intel Core i7 processor with 16GB of RAM.

	Convolution Threshold	1 sec	2 sec	5 sec	10 sec	15 sec	20 sec	30 sec	40 sec	full scan (47 sec)
16 GB	100	0.372	0.466	0.78	1.546	2.129	2.83	3.903	7.77	9.309
	150	0.266	0.369	0.749	1.414	2.009	2.69	3.943	6.887	7.73
	200	0.235	0.35	0.72	1.455	2.004	2.767	3.859	7.032	7.418
	250	0.222	0.353	0.718	1.418	1.975	2.676	4.007	6.717	7.426

CHAPTER 6. CONCLUSIONS

This research project demonstrated the current state-of-the-art for traffic network monitoring using a novel combination of three emerging technologies, unmanned aircraft system (UAS), light detection and ranging (lidar) and machine learning, and identified key avenues for ongoing work. An investigation of suitable remote aircraft and payloads for lidar-UAS traffic monitoring was conducted. A custom lidar-UAS was then built, instrumented, and used to collect data for multiple test sites, including a controlled test environment on the OSU campus, and a portion of the Newberg-Dundee construction site in Dundee, Oregon. Additionally, a higher-end UAS lidar, with greater range and higher georeferencing accuracy, was used to acquire data for a section of roadway near the University of Washington campus. All flights were conducted under FAA Part 107 regulations with Part 107 certified remote pilots serving as Pilot in Command (PIC).

Processing algorithms were developed to automatically parse raw data, generate georeferenced point clouds, filter out repetitions, and perform scanning to identify vehicles. Importantly, the software uses a pipelining process to sequentially scan each batch of collected data during any interval while the next batch is being collected, enabling efficient processing that could occur onboard the UAS. This work resulted in an end-to-end processing system, implemented in C++, capable of real-time vehicle recognition with processors that can be mounted on UAS.

The UAS data collection portions of the project were used to develop a set of operational recommendations for the use of UAS in traffic network monitoring. These recommendations are summarized in Chapter 5.1 and were disseminated in a PacTrans "Success Stories" project, through a *UAS in Transportation* workshop held on the OSU campus (Parrish et al., 2018). Analysis of the vehicle recognition system applied to two datasets demonstrated that the proposed system: a) can be utilized with both moving and static vehicles; b) can achieve suitably high detection rates and low false alarm rates; and c) can be made efficient enough for real-time operation onboard a UAS. The amount of RAM utilized in the testing was not found to have a significant effect, in comparison with the processor utilized. Similar timing results were obtained with 2GB, 4GB, and 8GB RAM configurations, indicating the smaller on-board computers with lower power consumption can be selected.

Looking to the future, trends in miniaturization of GNSS, INS, and lidar should greatly assist in traffic network monitoring with lidar-equipped UAS. Smaller, lighter payloads with the same or better performance specifications will enable smaller UAS to be used and also increase endurance (i.e., flight time per battery), which is highly beneficial for monitoring. So-called "hybrid" UAS, which allow vertical takeoff and landing (VTOL) like a multirotor, but then convert to a fixed-wing/glider-type aircraft when airborne, may greatly enhance operational efficiencies. At the same time, anticipated regulatory changes are likely to ease some of the operational challenges in use of UAS for transportation applications. For example, proposed new rules, which are being evaluated by the FAA (FAA, 2019) would allow for nighttime flights and flights over people (nonparticipants) without waivers in some situations.

Follow-on research will contribute to the long-range vision for traffic network monitoring, utilizing a fleet of lidar-equipped UAS that cover very wide transportation network segments, perform real time processing, and communicate with one another and with a the traffic network cloud controller, informing real-time decisions. Leveraging the results of this project, specific recommendations for future research include: 1) testing the software developed in this research on boards with lower computational

power; 2) improving the point cloud and reference vehicle filtering and further reducing latency; and 3) investigating new types of remote aircraft with greater endurance (e.g., hybrid UAS). Additionally, it is recommended that transportation agencies implementing UAS programs remain active in providing input on changes to UAS regulations, which may lead to significant increases in operational efficiency for applications, such as traffic network monitoring.

References

Barlow, Z., A. Sova, D. Hurwitz, and M. Olsen, 2019a. Risky Driver Glances at Roadside Unmanned Aerial System Operations. *ITE Journal*, June, pp.38-42.

Barlow, Z., H. Jashami, A. Sova, D. Hurwitz, and M. Olsen, 2019b. Driver Distraction Due to Drones. *Transportation Research Part C: Emerging Technologies*, 108, pp.207-222.

Collins, C.A., G.T. Roberson, and S.A. Hale, 2018. FAA 14 CFR Part 107 for Commercial UAS and UAS as Agriculture Field Equipment: A Review for Agriculture Safety Standards. In *2018 ASABE Annual International Meeting* (p. 1). American Society of Agricultural and Biological Engineers.

El-Sheimy, N., 2017. Georeferencing component of lidar systems. In *Topographic Laser Ranging and Scanning*, (Shan and Toth, Eds.), CRC Press, Boca Raton, Florida, pp. 195-214.

Eren, F., Jung, J., Parrish, C.E., Sarkozi-Forfinski, N. and Calder, B.R., 2019. Total Vertical Uncertainty (TVU) Modeling for Topo-Bathymetric LIDAR Systems. *Photogrammetric Engineering & Remote Sensing*, 85(8), pp.585-596.

Federal Aviation Administration (FAA), 2016. 14 CFR Parts 21, 43, 61, 91, 101, 107, 119, 133, and 183: Operation and Certification of Small Unmanned Aircraft Systems, Department of Transportation, Available online: https://www.faa.gov/uas/media/RIN_2120-AJ60_Clean_Signed.pdf.

FAA, 2019. DOT UAS Initiatives. Available online: https://www.faa.gov/uas/programs_partnerships/dot_initiatives/

Filin, S., 2003. Recovery of systematic biases in laser altimetry data using natural surfaces. *Photogrammetric Engineering & Remote Sensing*, 69(11), pp.1235-1242.

Fonstad, M.A., J.T. Dietrich, B.C. Courville, J.L. Jensen, and P.E. Carbonneau. 2013. Topographic structure from motion: a new development in photogrammetric measurement. *Earth Surface Processes and Landforms*, 38(4): 421-430.

Gillins, D.T., C. Parrish, M.N. Gillins, and C. Simpson, 2018. Eyes in the Sky: Bridge Inspections with Unmanned Aerial Vehicles. Final Report for Project SPR 787, Oregon Department of Transportation. Available online: https://trid.trb.org/View/1502840

Glennie, C.L., A. Kusari, and A. Facchin, 2016. Calibration and Stability Analysis of the VLP-16 Laser Scanner. *ISPRS Annals of Photogrammetry, Remote Sensing & Spatial Information Sciences*, 9.

Grewal, M.S., Andrews, A.P. and Bartone, C.G., 2013. *Global navigation satellite systems, inertial navigation, and integration*. John Wiley & Sons.

Hurwitz, D.S., M.J. Olsen, and Z. Barlow, 2018. Driving Distraction Due To Drones: Final Report Agreement #31167 - Project 3. Oregon Department of Transportation. Available online: https://www.oregon.gov/ODOT/Programs/ResearchDocuments/Driving_Distraction_due_to_Drones.pdf.

Jozkow, G., C. Toth, and D. Grejner-Brzezinsk, 2016. UAS Topographic Mapping With Velodyne LiDAR Sensor. *ISPRS Annals of Photogrammetry, Remote Sensing & Spatial Information Sciences*, 3(1).

Kellner, J.R., J. Armston, M. Birrer, K.C. Cushman, L. Duncanson, C. Eck, C. Falleger, B. Imbach, K. Král, M. Krůček, and J. Trochta, 2019. New opportunities for forest remote sensing through ultra-high-density drone lidar. *Surveys in Geophysics*, pp.1-19.

Nayegandhi, A., and J. Nimetz, 2018. Airborne Topographic Lidar, Ch. 8. In *Digital Eelvation Model Technologies and Applications: The DEM Users Manual, 3rd Ed.* (Maune and Nayegandhi, Eds.), ASPRS, Bethesda, Maryland.

Otero, L.D., N. Gagliardo, D. Dalli, W. H. Huang, and P. Cosentino. Proof of Concept for Using Unmanned Aerial Vehicles for High Mast Pole and Bridge Inspections. No. BDV28 TWO 977-02, Florida Institute of Technology, 2015.

Parrish, C., 2018. UAS Basics for Transportation. UAS in Transportation Expo, July 30-31, Corvallis, Oregon. Available online: http://depts.washington.edu/pactrans/wp-content/uploads/2018/09/Parrish_UAS_Basics_for_Transportation.pdf

Parrish, C., R. Slocum, and C. Simpson, 2018. UAS in Transportation Expo Final Report. Available online: http://depts.washington.edu/pactrans/wp-content/uploads/2018/11/UAS-in-Transportation-Report.pdf

Petrie, G., and C.K. Toth, 2009. Airborne and Spaceborne Laser Profilers and Scanners, Ch. 2, In *Topographic Laser Ranging and Scanning*, (Shan and Toth, Eds.), CRC Press, Boca Raton, Florida, pp. 195-214.

Phoenix LiDAR Systems, 2019. miniRANGER-UAV specifications sheet. Available online: https://www.phoenixlidar.com/miniranger/

Simpson, C., Parrish C., Sorour S., Abdel-Rahim A., Hurwitz D., 2017. Airborne lidar Scanning and Deep Learning System for Real-time Event Extraction and Control Policies in Urban Transportation Networks. Pacific Transportation Consortium (PACTRANS) Region 10 Conference (Poster Session), 6 October, Seattle, Washington.

Simpson, C., C. Parrish, D. Gillins, M. Gillins, E. Cain, and C. Glantz, 2018. Unmanned Aircraft Systems (UAS) for Bridge Inspection. Oregon GNSS Users Group Meeting, 19 June, Bend, Oregon.

Simpson, C., 2018. A Multivariate Comparison of Drone-Based Structure from Motion and Drone-Based lidar for Dense Topographic Mapping Applications. Oregon State University, 14 November, Corvallis, Oregon. Available online: ir.library.oregonstate.edu/concern/graduate_thesis_or_dissertations/q524jv207

Simpson, C., C. Parrish, D. Gillins, and M. Gillins, 2018. Lessons Learned from OSU PacTrans and ODOT UAS Projects. UAS in Transportation Expo, July 30-31, Corvallis, Oregon. Available online: http://depts.washington.edu/pactrans/wp-content/uploads/2018/09/Simpson_Lessons_Learned_from_PacTrans_ODOT_Projects_Small-compressed.pdf

Stöcker, C., R. Bennett, F. Nex, M. Gerke, and J. Zevenbergen, 2017. Review of the current state of UAV regulations. *Remote sensing*, 9(5), p.459.

Tonkin, T.N., N.G. Midgley, D.J. Graham, and J.C. Labadz. 2014. The potential of small unmanned aircraft systems and structure-from-motion for topographic surveys: A test of emerging integrated approaches at Cwm Idwal, North Wales. *Geomorphology* 226: 35-43.

Velodyne, 2018. *VLP-16 Velodyne LiDAR Puck: User's Manual and Programming Guide*. Velodyne LiDAR, Inc., Morgan Hill, California.

Westoby, M.J., J. Brasington, N.F. Glasser, M.J. Hambrey, and J.M. Reynolds. 2012. 'Structure-from-Motion' photogrammetry: A low-cost, effective tool for geoscience applications. *Geomorphology* 179: 300-314.